



Influence of Build Direction on the Fracture Mechanism of 3D Printed Octet Lattices

Thomas Draper , Dhruva Dayal, Susanta Ghosh , Trisha Sain**

*Department of Mechanical Engineering-Engineering Mechanics,
Michigan Technological University
Houghton, Michigan, United States, 49931*

Abstract

We investigate the effects of 3D printing build directions on the fracture properties of octet lattice metamaterials made of polylactic acid (PLA) and how these effects vary with the relative density of the lattices. Single-edge notch bend samples are 3D printed in two orthogonal build directions at various relative densities. Our results show that the work of fracture for octet lattices with build directions parallel to the crack plane is significantly higher than those with build directions perpendicular to the crack plane. We also observed that the ratio of specific work of fracture between the two build directions remains nearly constant across different relative densities. In contrast, the ratio of peak load between the two build directions decreases as relative density increases. Furthermore, the build direction dictates the fracture mechanism. While the perpendicular build direction predominantly results in a brittle (mode I) fracture, the parallel build direction leads to a complex, delamination-dominated (mode II type) fracture. This phenomenon is largely governed by the weak interfaces formed between the printed layers and their interaction with the lattice geometry. These results reveal that the build direction governs the fracture mechanism and work of fracture of these lattice metamaterials and is therefore an important design consideration.

1. Introduction

Lattice metamaterials have gained significant attention in the last decades due to their lightweight nature and tunable mechanical properties. Recent studies on lattice structures have unveiled unique mechanical properties such

*Email: susantag@mtu.edu

**Email: tsain@mtu.edu

as negative Poisson’s ratio [1], large surface area [2], high strength-to-density ratio [3], tunable stiffness [4], twisting under uniaxial forces [5], negative compressibility [6], and extraordinary resilience [7]. Due to the design programmability, any mechanical property of lattice materials can be tuned for their specific application making them an attractive option for use in load-bearing applications. Applications for lattice materials span industries such as medical [8], aerospace [9], automotive [10], etc [11]. Some specific applications include reducing the stiffness of metallic medical implants to match the stiffness of bone [12], light weighting sports equipment [13], and the core of sandwich panels [14].

In the last few years, advancements in additive manufacturing techniques have facilitated the manufacturing of lattice materials. While 3D printing methods like fused deposition modeling (FDM) [15] offer unique advantages for manufacturing complex geometries, such as lattice metamaterials, the mechanical properties are found to be highly dependent on the build direction and raster pattern. These factors induce anisotropy [16–18] and result in a large number of defects in the 3D printed objects, such as micro-voids. Additionally, the printing process induces differential cooling between the layers affecting inter-layer adhesion [18, 19].

Many lattice structure topologies have been investigated, however, lattices comprised of stretching-dominated unit cells are stronger and stiffer than those comprised of bending-dominated unit cells [3]. Such stretching-dominated structures include two-dimensional (2D) triangular or three-dimensional (3D) octet unit cells which are nearly isotropic [20]. The octet unit cell is stronger and tougher than most metallic and polymeric foams, with strength and toughness similar to wood loaded parallel to the grain [21]. The compressive strength and stiffness of the octet unit cell have been shown to scale linearly with the relative density [20]. Recent works have also revealed that the fracture toughness of the octet lattice scales linearly with relative density and with the square root of the strut length [21].

To improve the fracture toughness and damage resistance of lattice structures, many efforts have focused on designing lattices with bio-inspired toughening mechanisms such as introducing disorder [22], architected porosity [23], hierarchy [24], interpenetrating multi-materials [25], interlocking mechanisms inspired by the natural nacre of mollusk shells [26, 27], crack arrest and deflection [28], etc. While these design methods have shown promise in increasing toughness, the toughening mechanism typically requires more complex manu-

facturing efforts. Additionally, these processes may not be suitable for large-scale manufacturing which limits the scope of their practical applications. This work studies the inherent toughening mechanisms specific to 3D-printed octet lattices.

While the mechanical properties, such as strength and stiffness, of 3D-printed octet lattices have been widely studied, there are only a few investigations on their fracture properties. In particular, the effect of build direction on the fracture mechanism is yet to be explored. It is well known that the inter-layer bonding characteristics in thermoplastics printed using fused deposition modeling depend on the temperature difference between the previously deposited layer and the currently extruded one [19]. This difference creates a weak interfacial bonding between the printed layers. Furthermore, the plane or alignment of these weak interfaces depends on the build direction. The orientation and the fracture properties of the weak interface as a result govern the fracture mechanism of the material printed by fused deposition modeling. While the effect of weak interfaces on the fracture mechanism has been studied for 3D-printed solid materials [16–18], the same remains an open question for lattice metamaterials. Hence, the complex interaction between the lattice microstructure and the weak interfaces on the failure mechanism of lattice metamaterials needs to be investigated. The present work experimentally investigates how the orientation of the weak interface affects the fracture mechanisms of 3D-printed octet lattice metamaterials.

The organization of the rest of the paper is given below. In section 2.1, details of the manufacturing are presented. Sections 2.2 and 2.3 summarize the sample preparation, testing procedures, and fracture energy calculations. In section 3.1, the analysis of the load carrying capacity is presented, followed by in-situ image analysis of experiments and post-processing of load-displacement results in section 3.2. Furthermore, section 3.3 discusses trends in the specific work of fracture of the lattice metamaterials with respect to build direction. The initiation toughness of the lattices is discussed in section 4. Finally, the conclusions are presented in section 5.

2. Experimental details

In this section, we summarize the manufacturing and sample preparation, testing methods, and fracture energy formulation.

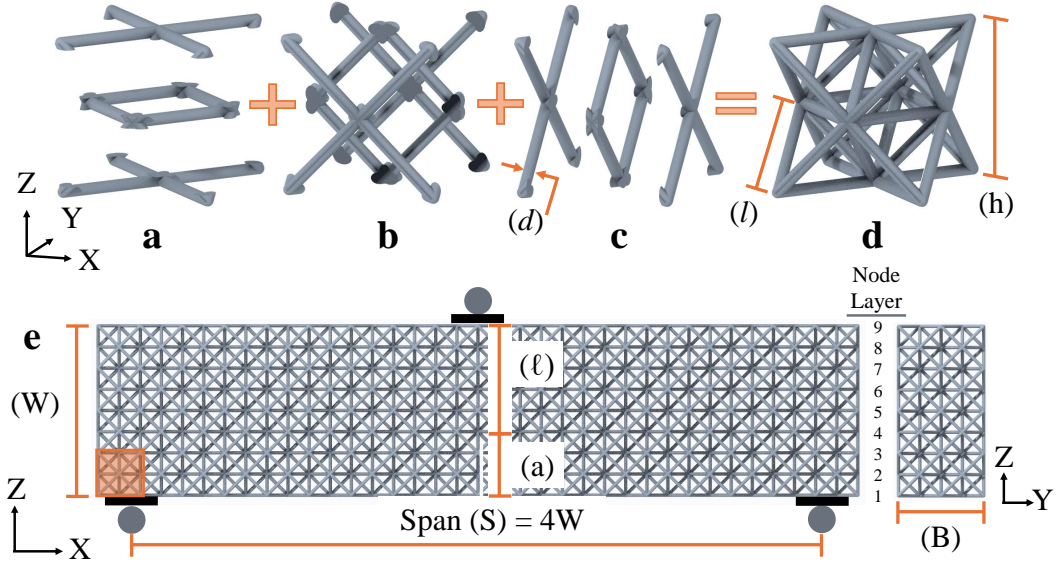


Figure 1: Schematic illustration of the octet unit cell (a)-(d) where (a) is the XY (horizontal) layers (b) is the XZ layers, (c) is the YZ (vertical) layers, and (d) is the full octet unit cell. (e) Fracture sample made up of $2 \times 4 \times 18$ unit cells where the node layer defines the numbers of the XY layers in the lattice. One unit cell is highlighted in orange. Parameters defined in the figure correlate to the following: strut diameter (d), strut length (l), unit cell height (h), width (W), ligament length (ℓ), notch length (a), span (S), and thickness (B)

2.1. Fracture sample preparation

This work examines single-edge notch bend (SENB) specimens made of octet lattices, shown in figure 1, which conform to the standard geometric requirements in ASTM E1820-23b [29]. ASTM E1820-23b is written for solid materials and thus does not specify a standard procedure to determine the minimum number of unit cells in a lattice necessary to determine the toughness. In a recent study, O'Masta et. al. performed finite element simulations and found that four unit cells across the width of the SENB fracture samples are sufficient to avoid over-estimation of the toughness. Following this, the fracture samples in this study are sized to $2 \times 4 \times 18$ unit cells which can be seen in figure 1(e).

The relative density, $\bar{\rho}$, of lattice structures is a key parameter in characterizing the mechanical properties. It relates the density of the lattice structure to the density of a solid of the same size and material. This study examines five relative densities characterized by the ratio of d/l . In this work, $\bar{\rho}$ is varied by fixing the strut length, l while varying the strut diameter, d . This method of changing the relative density ensures the quality of the struts in the 3D printing process while fixing the global size of the samples.

The SENB fracture samples are 3D printed on a Lulzbot TAZ 6 FDM printer equipped with a 0.5 mm diameter hardened steel nozzle. The samples are made from a Hatchbox PLA with a filament diameter of 3.00 mm. The specific printing parameters can be found in Appendix D. In summary, the nozzle and bed temperatures are 210°C and 65°C, respectively. The printing speed is set to 30 mm/s for all operations except the first layer, where 15 mm/s is used for better print bed adhesion. Each layer height is 0.25 mm and all printing is considered 100% infill. Lastly, the cooling fans are set to 100% for the duration of the print.

The initial notch in the samples is created using a band saw equipped with a 0.060-inch blade. The notch is terminated after cutting through the first three node layers as depicted in figure 1. Due to the high density of the lattices, the notch could not be terminated in the void space of a unit cell, as in [21]. Instead, the notch is terminated in the bulk of the struts past the third node layer. The location of the notch along the span of the SENB specimen could not be in the center as there are vertical struts in the centerline. Instead, the notch was cut immediately to one side of the centerline struts as done in [21]. See figure C.16 for a detailed look at the notch before testing. Though the unit cell height (h) for all $\bar{\rho}$ tested in this work is the same, the initial notch length varied slightly due to the varying strut diameter (d). The initial notch length (a) is defined by $a = h + d$.

Two mutually orthogonal build directions are considered in the printing and samples are tested under mechanical loading. The build direction of the so-called perpendicular samples is considered to be perpendicular to the initial notch, while the build direction of the parallel samples is parallel to the initial notch. Figure 2 depicts the nomenclature of the build direction of the samples.

The relative density is determined by measuring the mass of each lattice and dividing it by the mass of a printed solid of the same size, shape, and material printed with the same parameters as the octet lattices as described by the following equation:

$$\bar{\rho} = \frac{m_{lattice}}{m_{solid}} \quad (1)$$

where $m_{lattice}$ and m_{solid} are the mass of the octet lattice and solid respectively.

Table 1 summarizes the sample dimensions, microstructural size, and relative densities for all samples tested in this work (for more information on microstructure size, see table C.2 in Appendix C). The unit cell size, which determines the overall size of the SENB samples, was restricted by the print volume of the Lulzbot TAZ6. The smallest diameter of the struts is determined

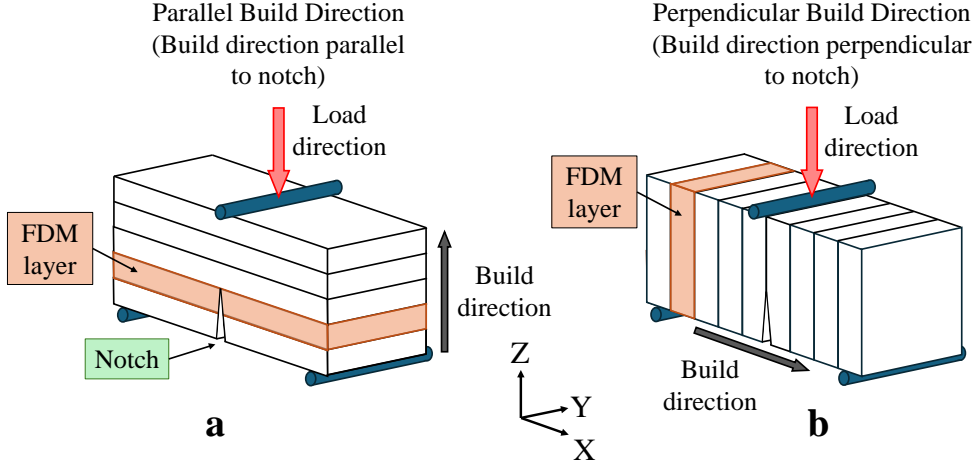


Figure 2: Nomenclature for build direction presented in this work is parallel direction (a) and perpendicular direction (b)

$\bar{\rho}$	$d(\text{mm})$	$l(\text{mm})$	$h(\text{mm})$	Number of unit cells	Measured dimensions (mm^3)
27%	2.00	8.84	12.5	$2 \times 18 \times 4$	$27.1 \times 226.6 \times 52.0$
33%	2.38	8.84	12.5	$2 \times 18 \times 4$	$28.0 \times 227.7 \times 53.0$
45%	2.75	8.84	12.5	$2 \times 18 \times 4$	$27.7 \times 227.4 \times 52.7$
51%	3.12	8.84	12.5	$2 \times 18 \times 4$	$27.9 \times 227.7 \times 53.0$
61%	3.50	8.84	12.5	$2 \times 18 \times 4$	$28.6 \times 227.9 \times 53.0$

Table 1: Fracture sample and unit cell dimensions. Parameters defined in the table are as follows: relative density ($\bar{\rho}$), CAD modeled strut diameter (d), CAD modeled strut length (l), CAD modeled unit cell height (h).

based on the 3D printer resolution. Three samples of each relative density and build direction are printed and tested to ensure consistency in the results.

2.2. Fracture testing

The fracture samples are then tested in three-point bending on an Instron TT-D testing frame equipped with an Instron 10,000 lb reversible load cell at room temperature. The three-point bending fixture is equipped with 1/4 inch bearings and set to a span of four times the specimen width, as specified by ASTM E1820-23b which varies with the relative density of the samples as shown in table 1 [29]. Due to the poor impact resistance of PLA, load spreaders are utilized to avoid local indentation from the bearings as is common in recent studies [7, 30] (as shown in figure 1). Samples are tested at a constant crosshead displacement rate of 1.5 mm/min to ensure a consistent quasi-static

strain rate. An MTS extensometer is placed into the notches and attached with rubber bands to record the crack mouth opening displacement (CMOD). Crosshead displacement, load, CMOD, and time are recorded during each test at a sampling frequency of 10 Hz. Tests are manually stopped after the load dropped below at least 50% of the peak. Further explanation of this is discussed in Section 2.3.

2.3. Fracture energy calculation

To capture both energy absorption during crack propagation and resistance to crack initiation, we consider two forms of toughness calculations that highlight different aspects of the material’s resistance to fracture. The first method is the essential work of the fracture method which is utilized to incorporate the large energy absorption of parallel lattices as a result of delamination behavior. The second method is to calculate the resistance to crack initiation, which is based on the linear elastic fracture mechanics assumption.

The essential work of fracture method was developed by Cotterel and Reddel in 1977 [31]. This method considers the fracture energy of a material, W_f , which is the area under the load-displacement curve. W_f is proportional to the ligament area, $\ell \cdot B$, where ℓ and B are defined in figure 1 as described by the following equation

$$w_f = \frac{W_f}{(\ell \cdot B)} \quad (2)$$

where w_f is the specific work of fracture. This is a simple experimental method to quantify fracture energy metrics that correlate to, but are not equal to, the fracture toughness of the structural material.

While the work of fracture method commonly reports the specific work of fracture for fully fractured samples, the present study considers the area under the load-displacement curve calculated once the load has dropped 50% from the peak load. This approach is chosen because a few samples in this work did not reach a fully fractured state within a reasonable amount of load-line displacement, as evidenced by significant plateaus in the load-displacement curve (figure 4). Hence, we decide that a 50% load drop represents a reasonable amount of crack propagation and energy dissipation to compare the work of fracture between the build directions. Therefore, the specific work of fracture is calculated based on a 50% load reduction, as seen in figure 3.

Our experiments reveal that crack propagation paths depend on the printing build direction. Perpendicular lattices exhibit brittle mode I fracture, whereas parallel lattices undergo complex delamination mechanisms. This se-

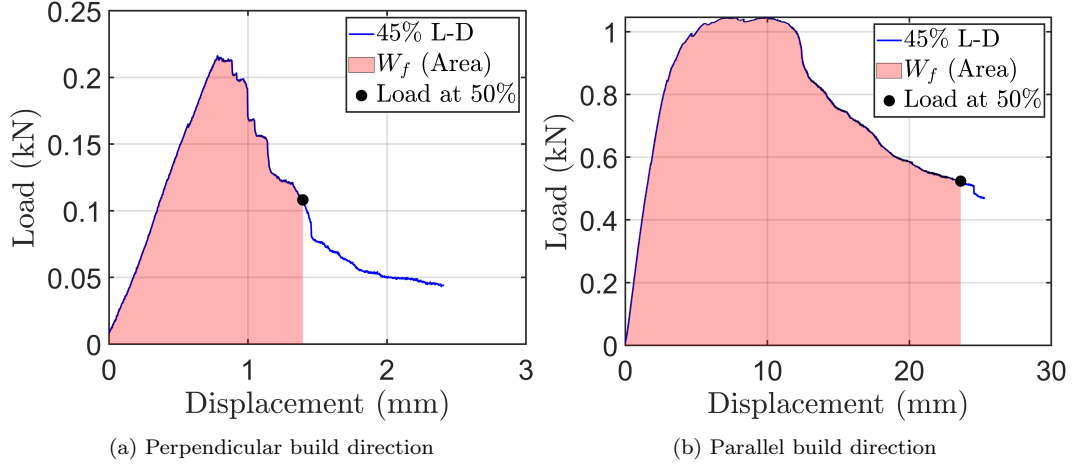


Figure 3: Area under the curve up to 50% load drop is shaded in red for (a) perpendicular and (b) perpendicular build directions for $\bar{\rho} = 45\%$.

ries of delamination complicates the calculation of traditional linear elastic fracture mechanics (LEFM) parameters, such as the critical stress intensity factor (K_{IC}) or the critical energy release rate (G_C). Crack length (a) must be estimated throughout the post-peak regime using the CMOD and geometrical relations to characterize the R-curve behavior of parallel lattices. However, the series of delamination (not all being at the crack tip) in parallel lattices complicates these calculations. Hence, we consider that LEFM remains applicable to these lattices until crack initiation, enabling a comparison of the initiation toughness for both build directions.

The initiation toughness is calculated following methods in ASTM E1820-23b, based on which (K_{INI}) is written as follows

$$K_{INI} = \left[\frac{P_Q S}{\sqrt{B}(W^{3/2})} \right] f(a/W) \quad (3)$$

P_Q is determined from a 95% secant line derived from the elastic part of the load-line displacement curve and

$$f(a/W) = \frac{3(\frac{a}{W})^{1/2} [1.99 - (\frac{a}{W})(1 - \frac{a}{W})(2.15 - 3.93(\frac{a}{W}) + 2.7(\frac{a}{W})^2)]}{2(1 + 2\frac{a}{W})(1 - \frac{a}{W})^{3/2}} \quad (4)$$

3. Results and discussion

In this section, we summarize the results from experiments and discuss the effect that build direction has on the fracture mechanisms, peak load, and toughness of PLA octet lattices.

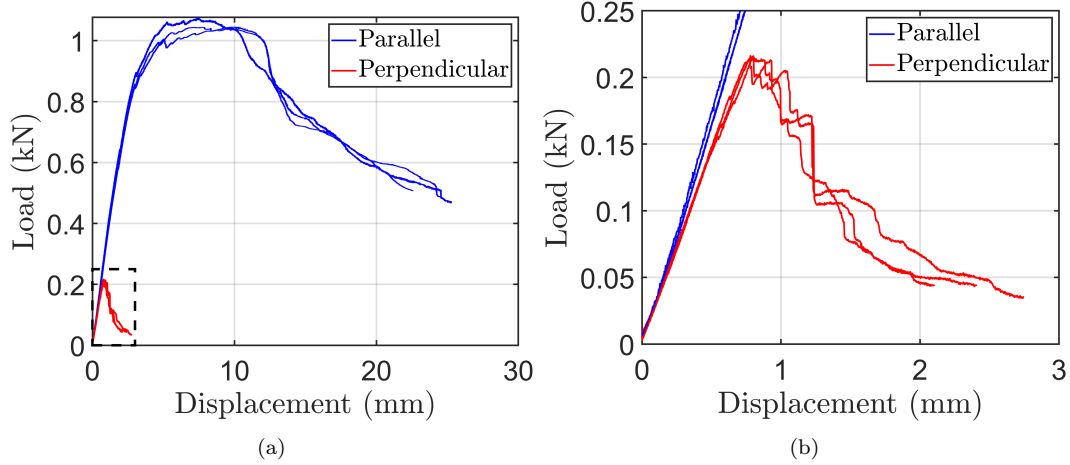


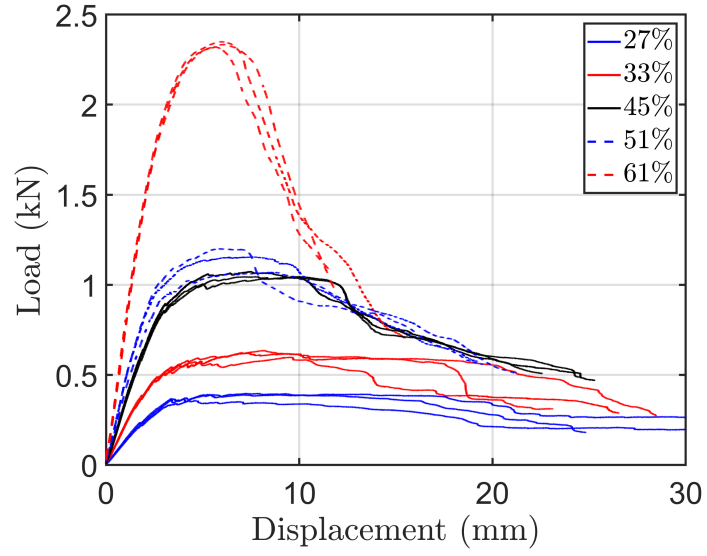
Figure 4: Load-displacement plot for $\bar{\rho} = 45\%$ parallel and perpendicular build directions plotted in blue and red respectively. Magnification in (b) represented by the black box in (a)

3.1. Effect of build direction on peak load

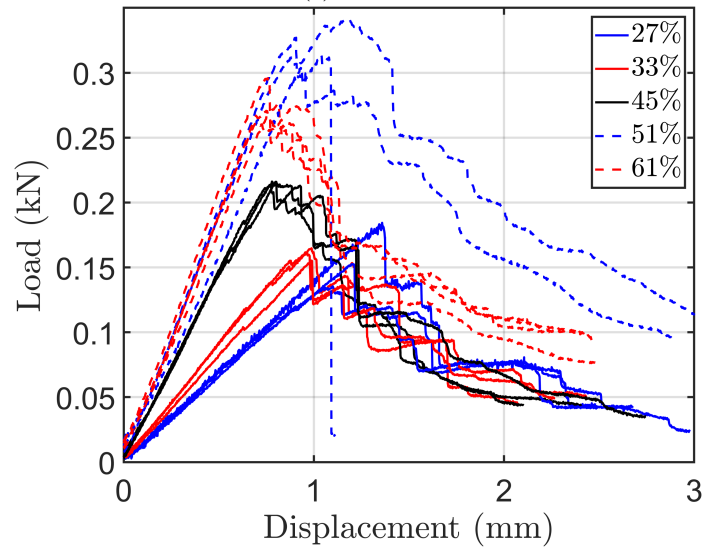
To investigate the effect of build direction on peak load, we analyze the load-displacement curves for the SENB specimen subjected to three-point bending. Figure 4 shows the load-displacement plots for one of the relative densities tested ($\bar{\rho} = 45\%$). The samples having a build direction parallel to the notch carry a significantly higher peak load compared to the perpendicular build direction (approximately 5 times).

To understand the above observation we focus on the strength of the interface between the build layers in the 3D printing process of the octet lattices. During the printing process, the PLA filament is melted and extruded through a nozzle, and deposited in a layer-by-layer fashion. This process yields weak interfaces between the printed layers¹. These weak interfaces are aligned along the notch of the sample for the perpendicular build direction, i.e. along the mode I fracture path of the sample, prompting the crack to propagate along the weak interfaces resulting in lower peak load. On the other hand, the interfaces are aligned perpendicular to the notch of the sample for the parallel build direction, i.e. perpendicular to the mode I fracture path of the sample. Therefore, for the crack to propagate along the mode I fracture path, the ap-

¹The extruded material in a layer adheres to the previously deposited layer and continues to cool until the next layer is extruded over it. The interface strength between consecutive layers depends on how much the previous layer has cured (cooled) with respect to the temperature of the current layer [19, 32]. This thermal gradient due to differential cooling creates a weak interface between the printed layers. According to [19], as the temperature difference between the layers increases, the inter-layer strength decreases.



(a) Parallel



(b) Perpendicular

Figure 5: Load-displacement plots for (a) parallel and (b) perpendicular octet lattice fracture samples. Relative density of each line is indicated in the legend.

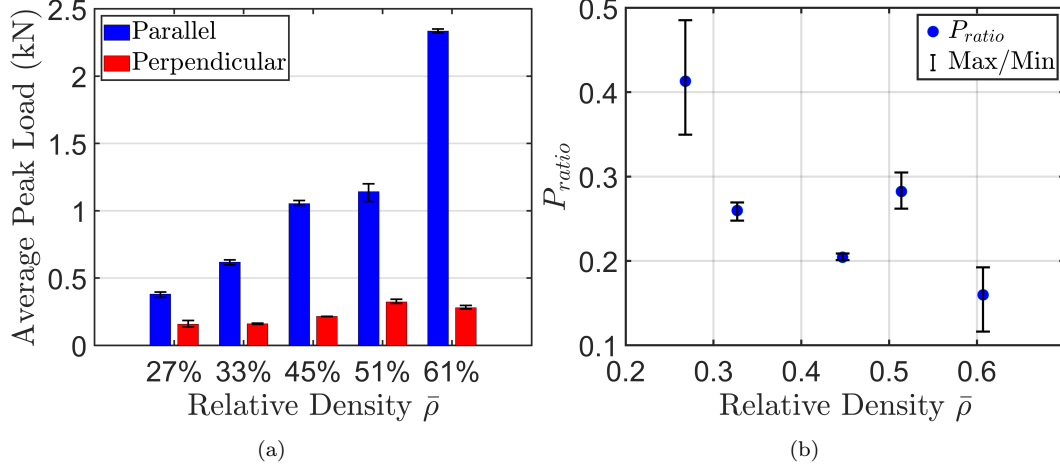


Figure 6: (a) Average peak loads for parallel and perpendicular build directions plotted over relative density. (b) Ratio of peak loads between parallel and perpendicular build directions. Error bars represent the minimum and maximum values.

plied load must overcome the ultimate tensile strength of the PLA fibers in the horizontal trusses, resulting in a higher peak load. These differing fracture mechanisms cause a large difference in peak load between the build directions.

To understand how the above trend (i.e. the large difference in peak load depending on the build direction) varies with relative density, five relative densities are considered. Figures 5 and 6 show the load-displacement curves and peak load summary for both build directions for various relative densities ($\bar{\rho}$). It is evident from these figures that as $\bar{\rho}$ increases, the peak load of the lattices also increase for both build directions, which is expected and consistent with current literature [21, 33]. For the perpendicular build direction, however, $\bar{\rho} = 51\%$ presents an outlier. Since the peak load is dependent on the strength of the (inter-layer) weak interface for the perpendicular build directions, multiple factors could induce premature failure or increased strength. These factors may include microvoids in the deposition causing stress risers, temperature conditions during printing affecting layer adhesion, humidity, etc. In contrast, the peak load of the parallel build direction is largely driven by the tensile strength of the PLA fibers in the horizontal trusses, hence shows a monotonic increase of peak load with $\bar{\rho}$.

3.2. Effect of build direction on fracture mechanisms

The experiments clearly demonstrate that the fracture behavior of the PLA octet lattice is strongly dependent on the build direction. In the following, we investigate the fracture mechanisms in detail for the two build directions.

The fracture images containing the crack propagation and delamination can be seen in figures 7 and 8 for parallel and perpendicular build directions respectively for various relative densities. It is evident from these figures that the damage in the parallel build direction can be characterized by two different failure mechanisms: delamination (mode II dominated fracture) and a ductile failure, while damage in the perpendicular build direction is dominated by brittle failure (mode I type fracture).

For the parallel build direction, a significant amount of delamination at the interface was observed near the crack-tip, as seen for the lower relative density samples in figure 7 ($\bar{\rho} = 27\%$ to 51%). These delaminations start at the crack-tip and advance to node layers ahead of the crack tip as the crack progresses². These delaminations occur at the nodes of the octet lattice where the intersection of the struts presents significant stress concentration. Note that delamination at the weak interface is also observed at the nodes for the aluminum snap-fit octet lattices, reported in [21]. To understand this delamination behavior, we explore the load transfer mechanism of the octet lattice and the presence of comparable T stresses in this lattice geometry. In the 3D lattice, the creation of a sharp notch is not practically possible. In those geometries, the so-called T-stress components are of finite values and scales with the crack tip mode-I stress intensity factor as noted in [34]. Hence, it could be possible that the magnitude of the T-stress is high enough to exceed the interfacial strength for the delamination (perpendicular to the crack front) to occur in the parallel lattice. In addition, the distributed delamination in several layers (ahead of the crack tip) can be explained by an intuitive 3D state of stress for a unit lattice. Since the octet lattice is a stretch-dominated unit cell the axial stresses in the struts are concentrated at the joints along the crack front plane. It could be possible that following the delamination right at the crack tip, the resolved shear stresses at the nodes in subsequent layers continue to exceed the strength of the weak interfaces causing a more stable fracture mode influenced by distributed delaminations.

To further understand the influence of microstructure and weak interfaces on the failure, we have also tested solid SENB samples, which are described in detail in Appendix B. Note that for the higher relative density lattice, the delaminations start at the nodes close to the notch tip, but do not propagate

²Node layers 4 and 5 as depicted in figure 1(e)

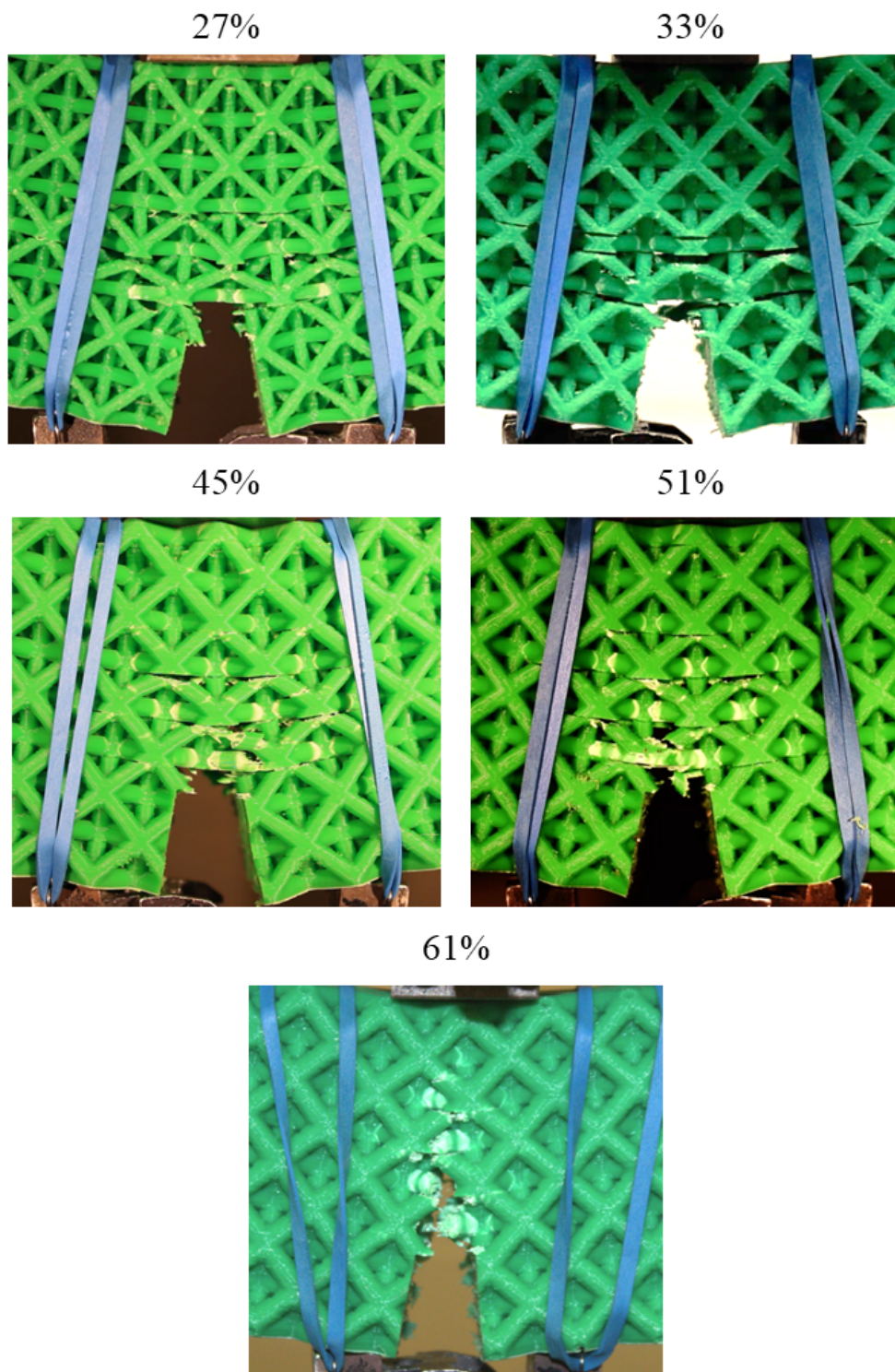


Figure 7: Fracture paths for parallel build direction having various relative densities

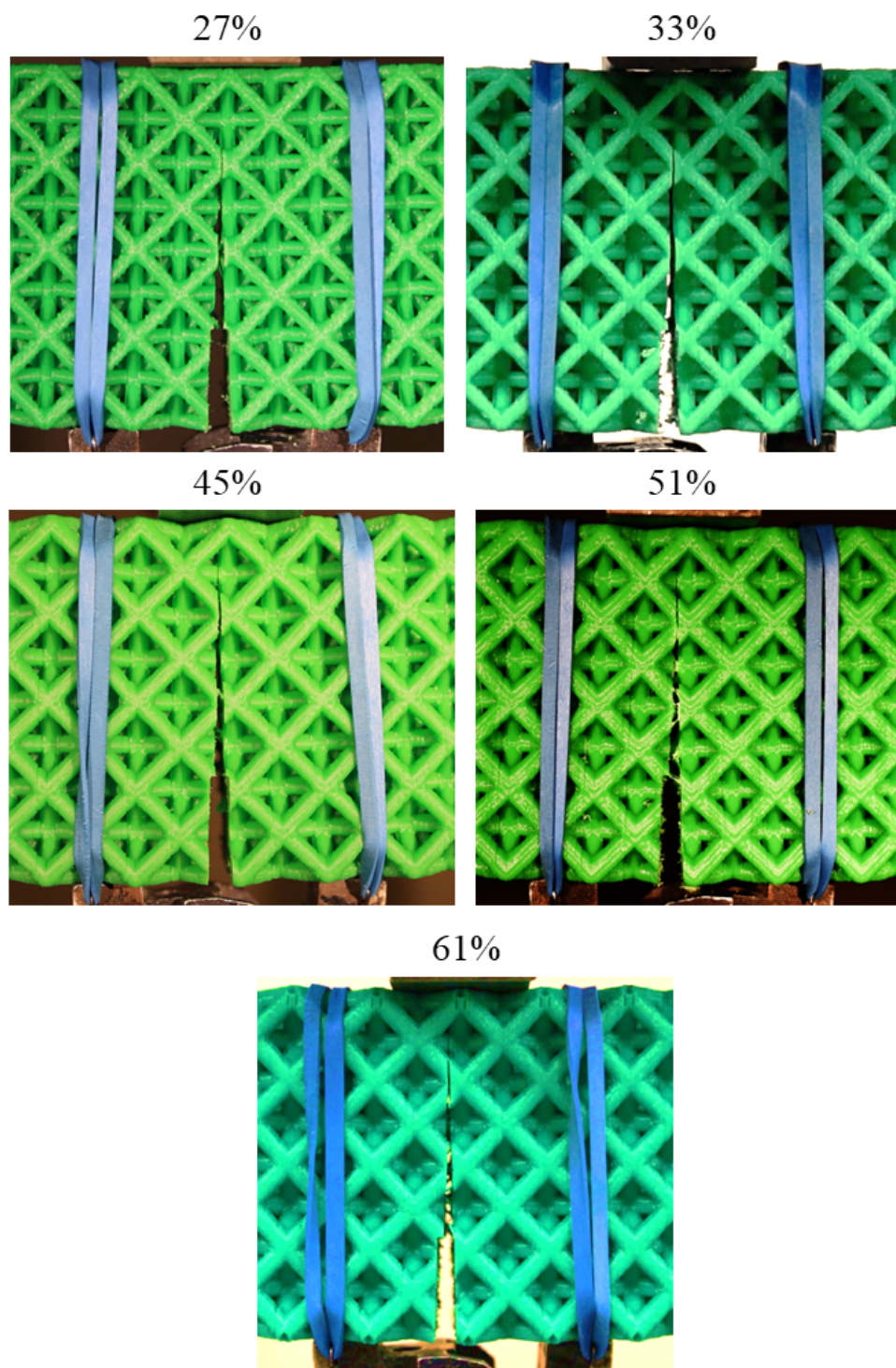


Figure 8: Fracture paths for perpendicular build direction having various relative densities

(along the weak interface) as much. Instead the struts fail under tension, as seen in figure 7 (for $\bar{\rho} = 61\%$). This is further explained in section 3.3.

The failure sequence of the parallel build direction is analyzed further to better understand the order of failure for relative density $\bar{\rho} = 27\%$. This sequence is depicted in figure 9. The load increased with displacement until the first node below the crack front delaminated at point (1) in figure 9(a). The lattice continued to carry the load until point (2), where the crack was arrested and deflected below node layer 4³. The delamination at point (2) is shown in figure 9(c). This image indicates that the failure occurred between the printed layers as the inter-layer strength was exceeded⁴. A series of local delaminations led to point (3), where joints below node layer 5 began to delaminate. Delamination continued between points (3) and (4) in the joints just below node layers 4 and 5, until the struts in horizontal layer 4 begin to yield and soften at point (4). This softening continued until ultimate failure at point (5), characterized by ductile failure of the struts at the nodes, as shown in figure 9(c). More local delamination in node layer 5 led to point (6) when layer 5 began to yield, after which the test was stopped. While this failure morphology is specific to one specimen, the combined failure mechanisms trend was consistent across all relative densities of the parallel build direction.

The failure of the perpendicular build direction is characterized by unstable mode I crack propagation aligned with the vertical trusses at the nodes of the lattices, as shown in figure 8 for all relative densities tested. The printed layers in the perpendicular build direction are aligned with the initial notch, and thus facilitate unstable crack growth through the weak interfaces. Note that for the perpendicular build direction, the relative density does not influence the crack path, since the weak interface drives the crack path.

To summarize, the fracture mechanisms of the octet lattices shift from brittle (mode I) to delamination-dominated (mode II) when the build direction shifts from perpendicular to the notch to parallel. In both cases, the crack propagates through the weak interfaces between the build layers of the 3D-printed lattices. The build layers in the perpendicular lattices align with the notch and promote mode I fracture, whereas the build layers in the parallel lattices are perpendicular to the notch causing crack arresting/deflection and promoting mode II-type fracture. While $\bar{\rho}$ does increase the strength and

³See figure 1(e) for node layer references.

⁴Further analysis of the inter-layer failure can be found in Appendix A

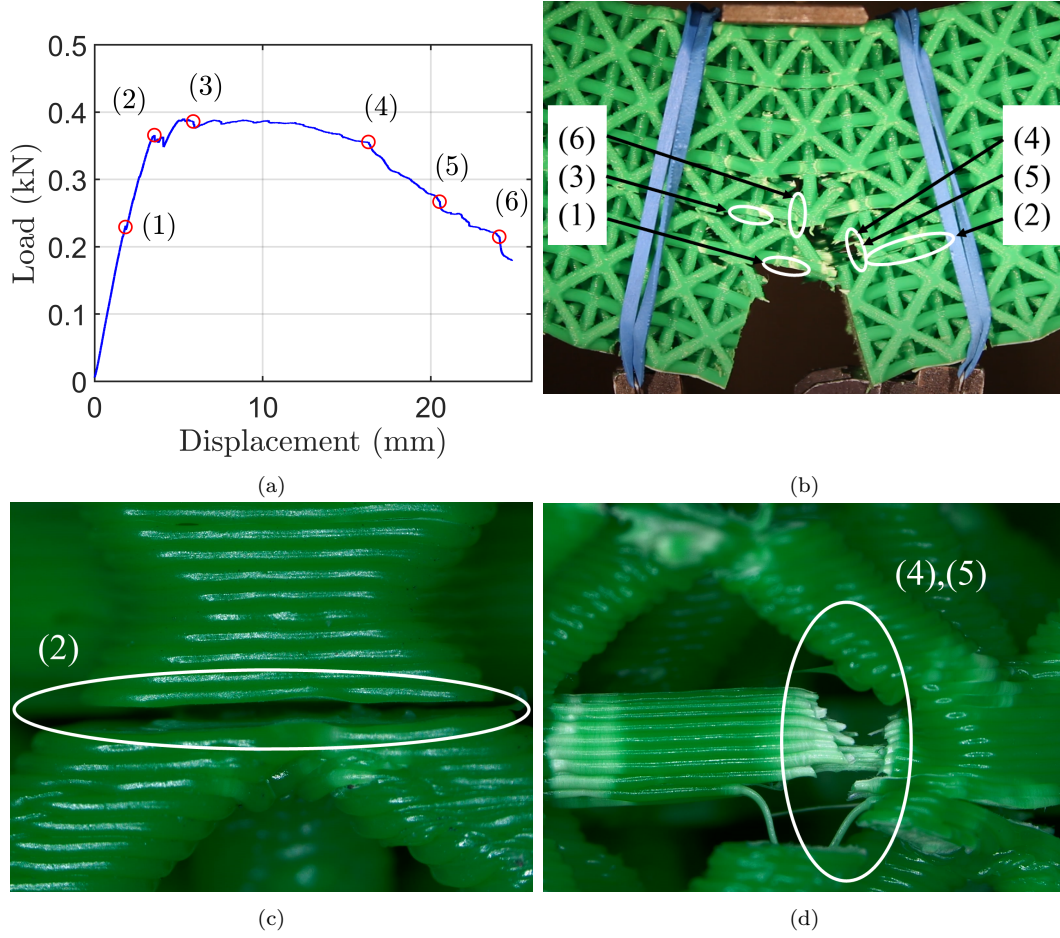


Figure 9: Failure evolution of a parallel lattice of $\bar{\rho} = 27\%$. (a) The load-displacement curve with points 1-6 denoting failure points on the lattice shown in (b). Magnified view of (c) mode II delamination and (d) ductile tensile failure of struts.

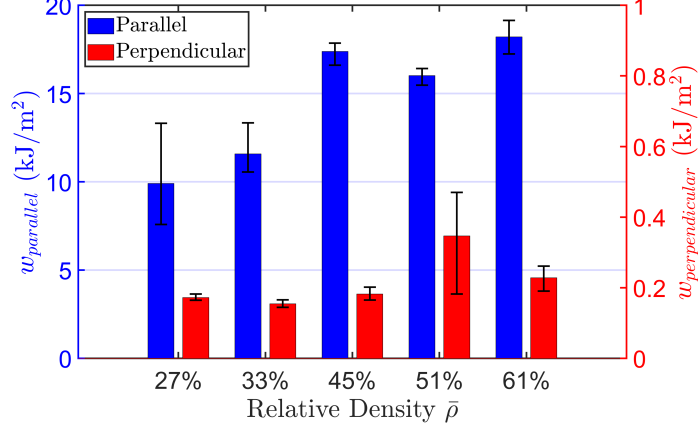


Figure 10: Average work of fracture for each build direction and relative density tested. Error bars represent maximum and minimum values. Left and right axis represent the scale for parallel and perpendicular build directions respectively

stiffness of the struts in the octet unit cell [20], this change in mechanical behavior of the struts does not impact the crack path. The crack path is instead influenced by competing mechanism of interfacial delamination and tensile failure of the struts.

It is to be noted that although the notch is located adjacent to a node, we do not anticipate significant changes in the results if the notch is placed at the midpoint between two nodes instead. This is because the dimensions of the SENB specimens are quite large relative to the microstructural characteristics, minimizing the sensitivity to the exact notch position. Our notch location follows the work of [21].

3.3. Characterizing toughness using work of fracture

Octet lattices printed with the build direction parallel to the notch absorb significantly more energy before fracture than perpendicular lattices. Figure 10 shows the computed average work of fracture values of the samples (note that parallel and perpendicular are plotted on separate axes). As discussed in section 2.3, the work of fracture is quantified by calculating the normalized area under the load-displacement curve up to 50% load reduction using Equation 2. The energy absorbed by the perpendicular lattices is about 2% of the energy absorbed by the parallel lattices.

To further understand how this trend varies with relative density, the ratio of the average perpendicular over parallel work of fracture is computed as follows:

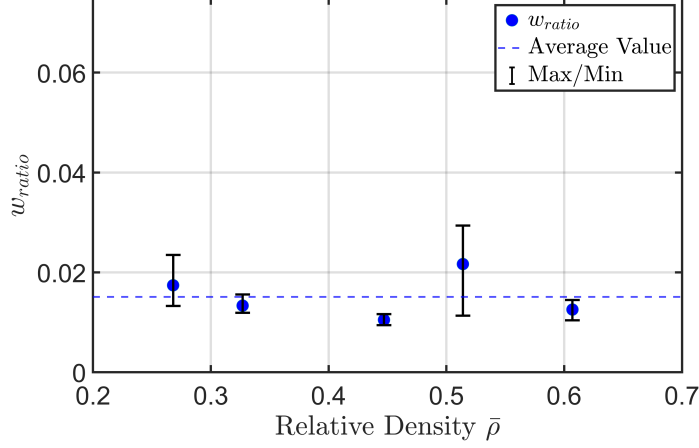


Figure 11: Work of fracture ratio, w_{ratio} , plotted over $\bar{\rho}$

$$w_{ratio} = \frac{w_{perpendicular}}{w_{parallel}} \quad (5)$$

Equation 5 is plotted in figure 11. This data suggests that the specific work of fracture ratio, w_{ratio} , remains constant. The $\bar{\rho} = 51\%$ sample is an outlier in this trend and can be attributed to the printing defects for the perpendicular lattices as discussed in section 3.1.

To explain why the average specific work of fracture of the parallel lattices is significantly higher than the perpendicular lattices, a similar discussion of the interlayer adhesion in section 3.1 can be referred to. The weak interface induced by the 3D printed layers is perpendicular to the initial notch in the parallel lattices, prompting a delamination-driven fracture. This delamination acts as a crack-arresting mechanism for the parallel lattices and significantly increases the toughness of the lattice geometry. This mechanism combined with the increased strength in the parallel lattices impacts the calculated specific work of fracture. The perpendicular lattices, however, undergo brittle mode I failure which correlates to low toughness. This mechanism combined with the lower strength in the perpendicular lattices causes lower specific work of fracture value compared to the parallel lattices.

To explain why the w_{ratio} remains constant with increasing $\bar{\rho}$, we must examine the fracture mechanisms of each build direction. As $\bar{\rho}$ increases in the parallel lattices, the fracture mechanism shifts from mode II delamination dominant to mode I ductile damage dominant. Such phenomenon of delamination as observed in low density lattices is common among layered materials when the interface presents a low-toughness fracture path introducing a mode II component leading to mode mixity [35]. It should be noted that a large body

of literature exists in this direction of analyzing mode mixity in heterogeneous materials containing interfaces, such as [35–37]. In those cases, mixed-mode crack propagation is prevalent, and the competition between crack propagation within the interface versus deflecting out of it depends on the relative toughness of the interface and the adjoining layers. Therefore, as the density increases in the parallel lattices, it is possible that the interfacial toughness increases compared to the fracture resistance offered by the struts in the adjoining layer. Hence, the propagating crack impinges on the lattice instead of the interface. This is also evident by comparing the mode II delamination in the low $\bar{\rho}$ and high $\bar{\rho}$ lattices in figure 7. The lower $\bar{\rho}$ lattices show significant delamination perpendicular to the initial notch while the higher-density lattices show minimal delamination. This trend is also evident when comparing the width of the plateau region of the load-displacement curves in figure 5a. As $\bar{\rho}$ increases, the width of the plateau region decreases, due to a transition from delamination dominated (mode II) to mode I crack propagation through the microstructure. We hypothesize two plausible explanations for this phenomenon. Firstly, the nodal volume increases with $\bar{\rho}$. A larger nodal volume requires more force to fracture the weak interface created by the 3D-printed layers. Due to this, the shear strength of the weak interface between the layers increases with increasing $\bar{\rho}$, and thus leads to mode I crack propagation through the microstructure compared to mode II delamination in the lower-density lattices. Since the nodal volume of the 33% samples is much smaller than the 61%, the shear strength of the weak interface is smaller, and the forces induced by the loading might exceed the shear strength of that weak interface quicker. Secondly, the higher-density samples have more thermal inertia during the printing process, due to the increase in mass of the lattice. The amount of heat loss decreases as the thermal inertia increases, which likely strengthens the bond between the printed layers. Consequently, the differential cooling effect for higher $\bar{\rho}$ samples is reduced, leading to better adhesion between the layers. This improved adhesion increases the inter-layer shear strength, causing the normal stresses at the notch tip to exceed the strength of the bulk PLA material in the struts before the shear stresses exceed the interface strength.

As discussed in Section 3.2, the perpendicular octet lattices fail in a brittle manner. Consequently, the specific work of fracture is driven by the strength of the lattices, as there is no crack-arresting mechanism to increase the toughness. The strength of the perpendicular lattices is driven by the inter-layer adhesion,

rather than the strength of the bulk PLA in the case of the parallel lattices. As discussed previously, the strength of the lattices increases with $\bar{\rho}$, which is also evident in the work of fracture trend for the perpendicular lattices.

While each build direction undergoes significantly different fracture mechanisms, the work of fracture of both parallel and perpendicular octet lattices increases with $\bar{\rho}$ at similar rates, and thus w_{ratio} remains independent of $\bar{\rho}$.

4. Characterizing fracture initiation toughness

Figure 12a plots the computed fracture initiation toughness (K_{INI}) of both build directions against the relative density of the lattices. As discussed in section 3.3, the initiation of crack extension is based on the intersection of a 95% secant line with the load-displacement curve consistent with the methods in ASTM E1820-23b. Note that for the parallel lattices, there is a significant amount of increase in load is observed after this P_Q limit which corresponds to a rising R-curve type behavior. From 12a it is seen that, the parallel lattices have a larger initiation toughness than that of the perpendicular lattices, which is consistent with the work of fracture trend, however less drastic. Additionally, both parallel and perpendicular lattices show an increase in K_{INI} with increasing $\bar{\rho}$ which is also consistent with recent studies [21].

The same initiation toughness calculations were performed on the solid SENB specimens and used as a normalization parameter for the lattices. Figure 12b shows a plot of normalized K_{INI} plotted over relative density for both build directions. The trend shown in this plot is consistent with aluminum snap-fit octet lattices of [21]. From this plot, we conclude that the trend in normalized initiation toughness is proportional to the relative density and independent of the build direction.

5. Conclusions

In this study, we investigate how the build direction influences the fracture behavior of 3D-printed PLA octet lattices. Fused deposition modeling-based lattice metamaterials are subject to the formation of weak bonding between the layers due to differential cooling during the print. We found that the build direction not only impacts the peak load of the lattice but completely alters the mode and mechanisms of fracture in single-edge notch bend specimens. Moreover, the investigation delves into the influence of relative density on both the toughness and peak load for the two build directions.

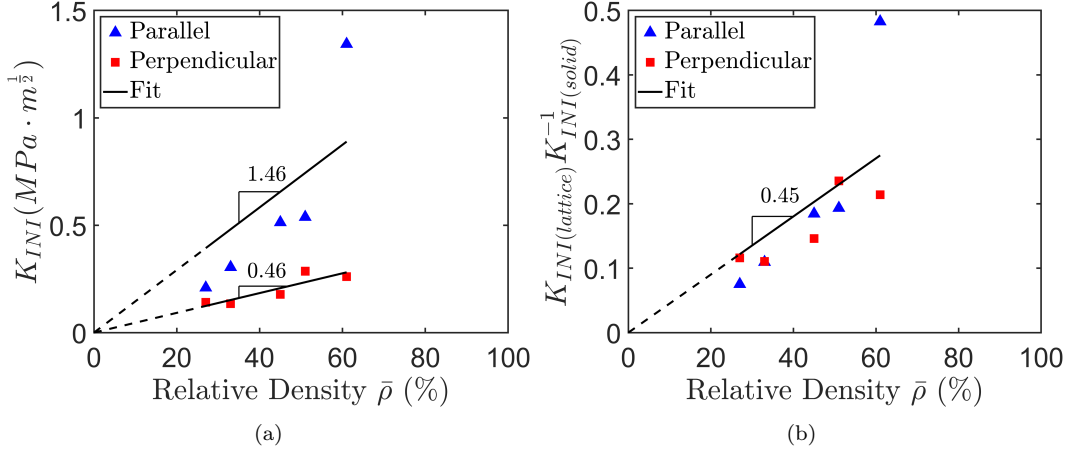


Figure 12: (a) Average initiation toughness (a) and average normalized initiation toughness (b) plotted over relative density.

To conclude this study, we summarize its main findings as follows- *Firstly*, the fracture mechanism of 3D printed PLA octet lattices is governed by the alignment of the weak interface induced by build direction. When the 3D printing build direction is parallel to the notch plane, the fracture is delamination (mode II) dominated followed by ductile failure of struts. The delamination follows the weak interface passing through the joints of the octet lattice. This fracture process yields significantly higher toughness. However, when the build direction is perpendicular to the notch, the weak interface in the lattices facilitates brittle (mode I) fracture along the notch path, resulting in significantly lower toughness. *Secondly*, the toughness for the build direction perpendicular to the notch is significantly lower, approximately 2%, compared to the build direction parallel to the notch. *Third*, the initiation toughness is proportional to the relative density and the normalized initiation toughness is independent of the build direction. *Fourth*, the toughness for both build directions increases with relative density, yet their ratio remains largely unchanged. *Finally*, as the relative density increases, the peak load for both build directions also increases as expected. However, their ratio shows a decreasing trend with higher relative density.

While this study explored the two most important mutually orthogonal build directions, future research will consider a variety of other printing directions. Additionally, various other printing parameters influencing the layer adhesion, including but not limited to, cooling fan percentage, nozzle temperature, the use of a heated or non-heated chamber, and print speed will be

explored. Lastly, investigating the effect of build direction on other lattice topologies, such as body-centered cubic, cuboctahedron, and open-cell Kelvin foam, would be an interesting research direction.

Acknowledgements

We acknowledge Ben Jewell and Dhruva Dayal for helping with the experiments, Jake Lundin for helping with the 3D printing, and Revanth Matthey for many insightful discussions on the fracture process. This research is supported by the Research Excellence Fund #2112019 from MTU. SG acknowledges financial support by grant DE-SC0023432 funded by the U.S. Department of Energy, Office of Science.

Appendix A.

The fractured octet lattices were further analysed using a Leica DVM6 A digital microscope to understand the inter-layer failure of the 3D printed struts/nodes. The Leica microscope consists of a PlanAPO FOV 43.75 lens where a max magnification of 190:1 can be obtained. Figure A.13 depicts microscopic images of the inter-layer fracture for both parallel and perpendicular lattices at low and high $\bar{\rho}$. Measurements of the printed layers surrounding the inter-layer fracture are taken to better understand the failure mechanism. The Leica LAS X software was utilized to take these measurements through careful adjustments of the microscope focus. It was found that the printed layers adjacent to the fracture on either side measure very close to 0.25 mm, which is the layer height the 3D printer was programmed to write. Slight variations of this dimension are noted and attributed to the heterogeneity of the printing process. This further supports the claims that fracture occurs between the layers, rather than in the bulk PLA fibers.

Appendix B.

In order to understand the difference between octet lattice failure and solid failure, the same SENB fracture tests were conducted on solids. Solid SENB samples of the same size and shape as the octet lattices were printed, prepared, and tested using the same parameters. Figure B.14 shows the load-displacement plots for all solids tested. There is still a large difference in peak load between the parallel and perpendicular build directions, similar to the

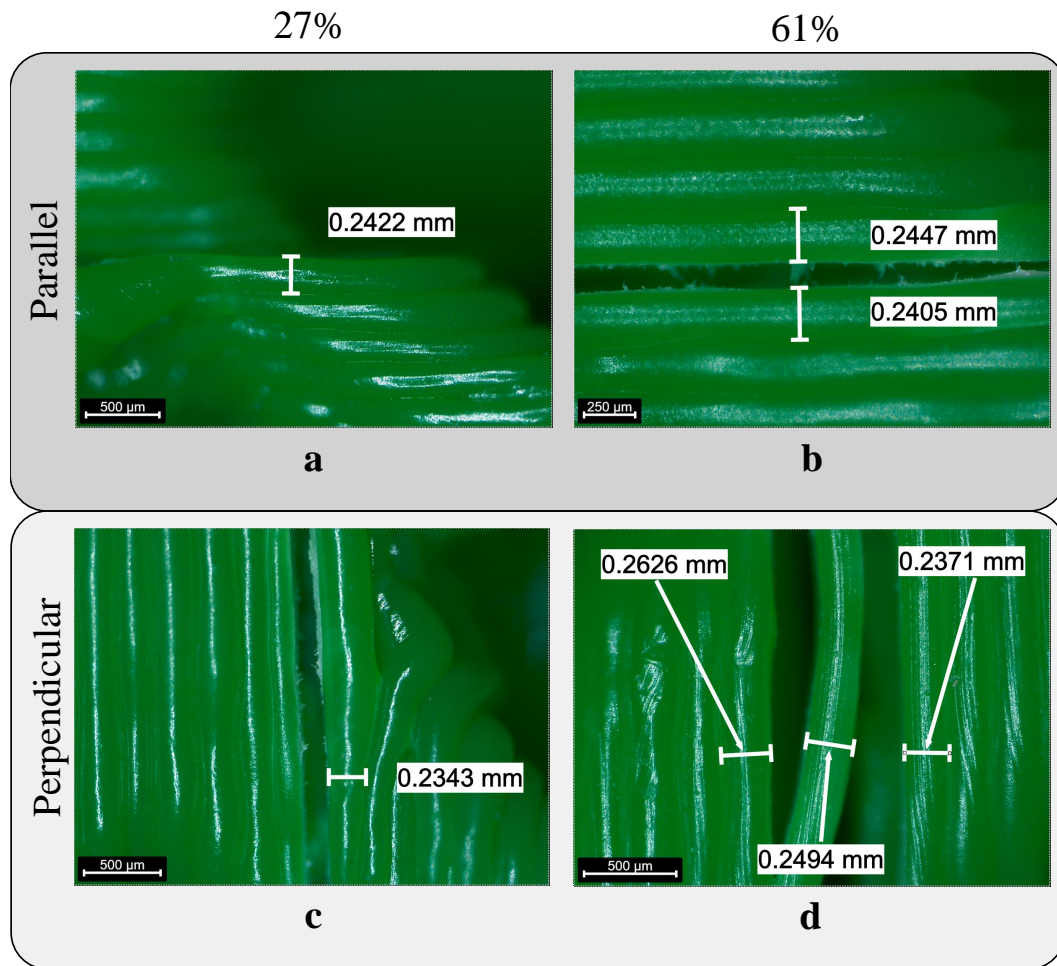


Figure A.13: Microscopic images of the inter-layer failure of (a) 27% parallel, (b) 61% parallel, (c) 27% perpendicular, (d) 61% perpendicular fracture samples. Measurements indicated in the figures are taken by the Leica LAS X software.

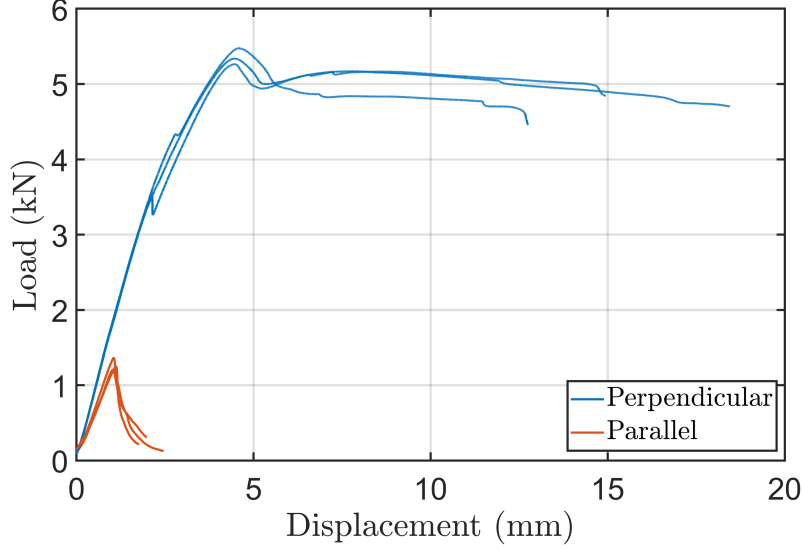
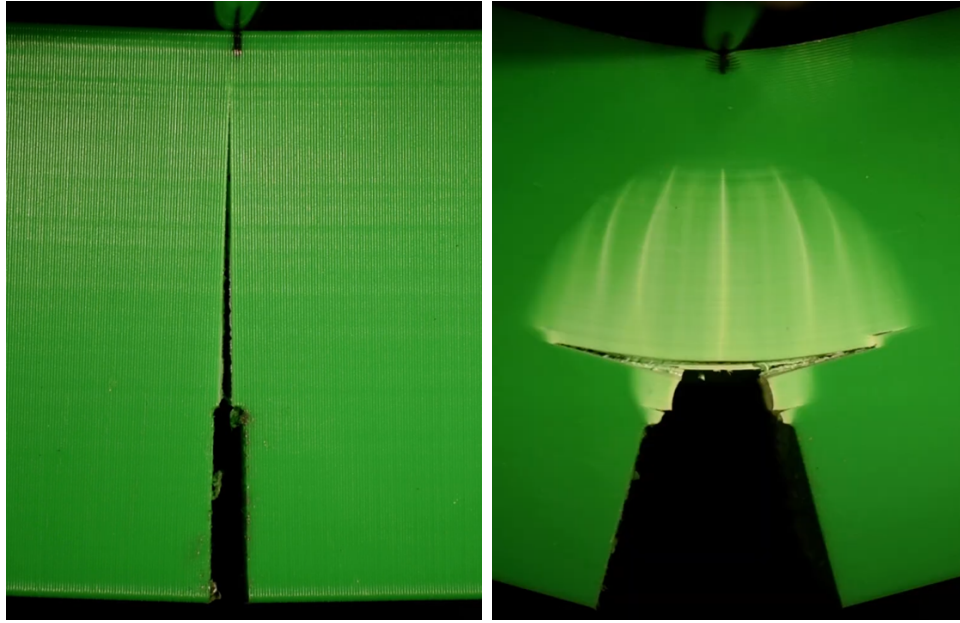


Figure B.14: Load-displacement curves of solid SENB samples for both perpendicular (red) and parallel (blue) oriented parts

octet lattice. Additionally, the large plateau section in the parallel solid represents a delamination fracture mechanism, which differs from the quasi-brittle response of the perpendicular solid.

The major difference between the solid SENB fracture and the octet lattice is the influence of the microstructure on the failure pattern of the struts. As shown in figure 9 and described in Section 3.2, the delamination in the parallel samples occurs above the crack front in the octet lattice. Additionally, sudden drops in load throughout the testing due to local failure of the octet lattice are evident. This differs from the failure of the solid where the crack propagates perpendicular to the printed layers until the crack is arrested and the solid delaminates continually at the crack front. This can be seen in figure B.15.



(a) Perpendicular

(b) Parallel

Figure B.15: In-situ fracture images of solid SENB fracture samples for (a) perpendicular and (b) parallel build directions

Appendix C.

Relative Density	Build direction	Sample number	Thickness [B] (mm)	Length (mm)	Width [W] (mm)
27%	Parallel	1	26.84	226.6	51.99
		2	26.97	226.6	52.00
		3	26.97	226.4	52.08
	Perpendicular	1	27.20	226.6	52.04
		2	27.19	226.7	52.04
		3	27.14	226.6	52.04
33%	Parallel	1	28.02	227.7	52.98
		2	28.02	227.6	52.93
		3	28.02	227.7	52.96
	Perpendicular	1	28.02	227.7	53.11
		2	28.04	227.9	52.96
		3	28.07	227.8	53.09
45%	Parallel	1	27.69	227.3	52.86
		2	27.71	227.4	52.50
		3	27.71	227.5	52.78
	Perpendicular	1	27.69	227.5	52.82
		2	27.69	227.4	52.72
		3	27.75	227.4	52.76
51%	Parallel	1	27.90	227.7	52.94
		2	27.88	227.6	53.07
		3	27.88	227.7	52.90
	Perpendicular	1	27.97	227.8	52.08
		2	28.06	227.8	52.13
		3	27.97	227.8	53.11
61%	Parallel	1	28.78	228.4	53.52
		2	28.83	228.4	53.25
		3	28.74	228.3	53.60
	Perpendicular	1	28.66	225.6	53.84
		2	28.17	228.3	52.02
		3	28.16	228.2	52.06

Table C.2: Global fracture sample sizes. Measurements were taken on The L.S. STARRETT CO. Hardened and stabilized Master Bar No. 254. Three measurements of each dimension were averaged to form the values in the table.

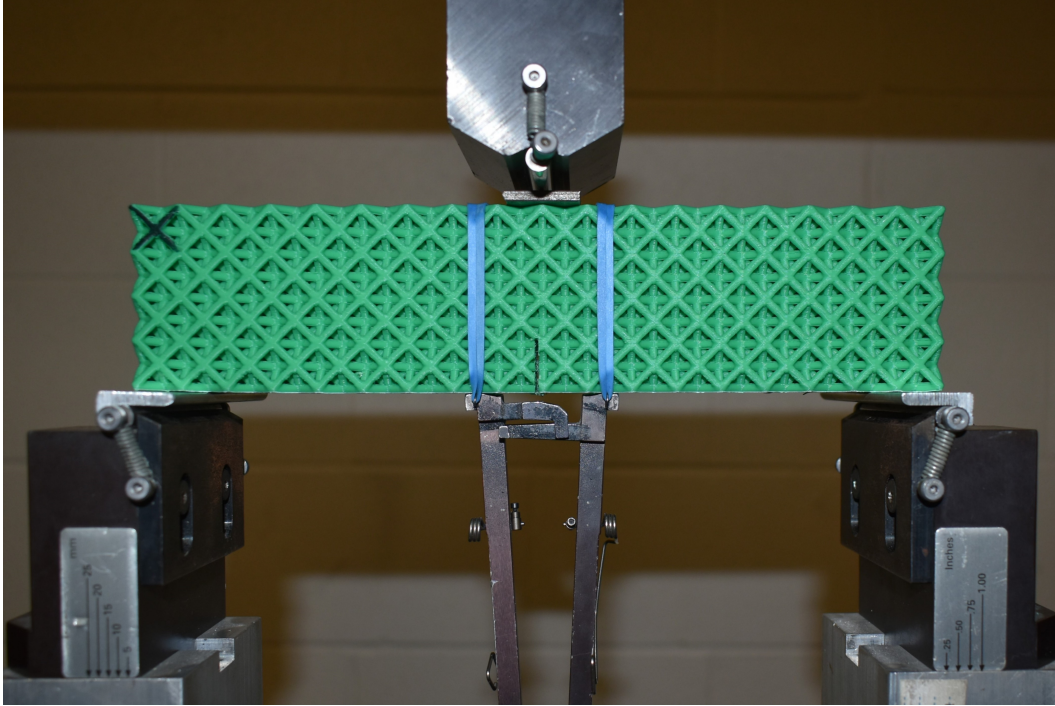


Figure C.16: SENB fracture sample setup on test fixture before testing.

Appendix D.

Setting	Profile	Unit
Layer height	0.25	mm
Initial layer height	0.25	mm
Build plate temperature	65	°C
Part Removal Temperature	45.0	°C
Keep heating	True	
Build plate temperature initial layer	65.0	°C
Combing mode	all	
Retract before outer wall	False	
Generate support	False	
Built plate adhesion type	brim	
Enable bridge settings	True	
Minimum bridge wall length	0	mm
Line width	0.5	mm
Wall thickness	1.0	mm
Top thickness	1	mm
Top layers	6	
Bottom thickness	1	mm
Infil before walls	False	
Printing temperature	205	°C
Retraction distance	1.75	mm
Retraction speed	10	mm/s
Outer wall speed	40	mm/s
Inner wall speed	45	mm/s
Top/bottom speed	40	mm/s
Travel speed	175	mm/s
Initial layer speed	15	mm/s
Regular/maximum fan speed threshold	30	s
Regular fan speed at height	2	mm
Minimum layer time	30	s
Skirt/brim minimum length	250	mm
Brim line count	10	
Raft air gap	0.5	mm
Initial layer Z overlap	0.5	mm

Table D.3: Print settings from Cura Lulzbot Edition slicing software

References

- [1] H. Wang, Y. Zhang, W. Lin, and Q.-H. Qin, “A novel two-dimensional mechanical metamaterial with negative poisson’s ratio,” *Computational Materials Science*, vol. 171, p. 109232, 2020.
- [2] N. Baobaid, M. I. Ali, K. A. Khan, and R. K. Abu Al-Rub, “Fluid flow and heat transfer of porous tpms architected heat sinks in free convection environment,” *Case Studies in Thermal Engineering*, vol. 33, p. 101944, 2022.
- [3] V. Deshpande, N. Fleck, and M. Ashby, “Effective properties of the octet-truss lattice material,” *Journal of the Mechanics and Physics of Solids*, vol. 49, no. 8, pp. 1747–1769, 2001.
- [4] L. Zheng, S. Kumar, and D. M. Kochmann, “Data-driven topology optimization of spinodoid metamaterials with seamlessly tunable anisotropy,” *Computer Methods in Applied Mechanics and Engineering*, vol. 383, p. 113894, 2021.
- [5] T. Frenzel, M. Kadic, and M. Wegener, “Three-dimensional mechanical metamaterials with a twist,” *Science*, vol. 358, no. 6366, pp. 1072–1074, 2017.
- [6] Z. G. Nicolaou and A. E. Motter, “Mechanical metamaterials with negative compressibility transitions,” *Nature Materials*, vol. 11, no. 7, pp. 608–613, Jul 2012.
- [7] L. R. Meza, A. J. Zelhofer, N. Clarke, A. J. Mateos, D. M. Kochmann, and J. R. Greer, “Resilient 3d hierarchical architected metamaterials,” *Proceedings of the National Academy of Sciences*, vol. 112, no. 37, pp. 11 502–11 507, 2015.
- [8] I. Zein, D. W. Hutmacher, K. C. Tan, and S. H. Teoh, “Fused deposition modeling of novel scaffold architectures for tissue engineering applications,” *Biomaterials*, vol. 23, no. 4, pp. 1169–1185, 2002.
- [9] H. Klippstein, A. Diaz De Cerio Sanchez, H. Hassanin, Y. Zweiri, and L. Seneviratne, “Fused deposition modeling for unmanned aerial vehicles (uavs): A review,” *Advanced Engineering Materials*, vol. 20, no. 2, p. 1700552, 2018.

- [10] S. L. Rahim and S. Maidin, “Feasibility study of additive manufacturing technology implementation in malaysian automotive industry using analytic hierarchy process,” in *Manufacturing Engineering*, ser. Advanced Materials Research, vol. 903. Trans Tech Publications Ltd, 5 2014, pp. 450–454.
- [11] J. U. Surjadi, L. Gao, H. Du, X. Li, X. Xiong, N. X. Fang, and Y. Lu, “Mechanical metamaterials and their engineering applications,” *Advanced Engineering Materials*, vol. 21, no. 3, p. 1800864, 2019.
- [12] E. Alabort, D. Barba, and R. C. Reed, “Design of metallic bone by additive manufacturing,” *Scripta Materialia*, vol. 164, pp. 110–114, 2019. [Online]. Available: <https://www.sciencedirect.com/science/article/pii/S1359646219300399>
- [13] A. Subic, *Materials in sports equipment*. Woodhead Publishing, 2019.
- [14] M. Khoshgoftar, A. Barkhordari, M. Limuti, F. Buccino, L. Vergani, and M. J. Mirzaali, “Bending analysis of sandwich panel composite with a re-entrant lattice core using zig-zag theory,” *Scientific Reports*, vol. 12, no. 1, p. 15796, 2022.
- [15] S. Daminabo, S. Goel, S. Grammatikos, H. Nezhad, and V. Thakur, “Fused deposition modeling-based additive manufacturing (3d printing): techniques for polymer material systems,” *Materials Today Chemistry*, vol. 16, p. 100248, 2020.
- [16] R. Zou, Y. Xia, S. Liu, P. Hu, W. Hou, Q. Hu, and C. Shan, “Isotropic and anisotropic elasticity and yielding of 3d printed material,” *Composites Part B: Engineering*, vol. 99, pp. 506–513, 2016.
- [17] J. Kiendl and C. Gao, “Controlling toughness and strength of fdm 3d-printed pla components through the raster layup,” *Composites Part B: Engineering*, vol. 180, p. 107562, 2020.
- [18] R. Matthey, B. Jewell, S. Ghosh, and T. Sain, “Phase-field fracture coupled elasto-plastic constitutive model for 3d printed thermoplastics and composites,” *Engineering Fracture Mechanics*, vol. 291, p. 109535, 2023.
- [19] H. R. Vanaei, K. Raissi, M. Deligant, M. Shirinbayan, J. Fitoussi, S. Kheladi, and A. Tcharkhtchi, “Toward the understanding of temperature ef-

- fect on bonding strength, dimensions and geometry of 3d-printed parts,” *Journal of Materials Science*, vol. 55, pp. 14 677–14 689, 2020.
- [20] V. Deshpande, M. Ashby, and N. Fleck, “Foam topology: bending versus stretching dominated architectures,” *Acta Materialia*, vol. 49, no. 6, pp. 1035–1040, 2001.
 - [21] M. O’Masta, L. Dong, L. St-Pierre, H. Wadley, and V. Deshpande, “The fracture toughness of octet-truss lattices,” *Journal of the Mechanics and Physics of Solids*, vol. 98, pp. 271–289, 2017.
 - [22] N. E. Romijn and N. A. Fleck, “The fracture toughness of planar lattices: Imperfection sensitivity,” *Journal of the Mechanics and Physics of Solids*, vol. 55, no. 12, pp. 2538–2564, 2007.
 - [23] K. M. Conway, C. Kunka, B. C. White, G. J. Pataky, and B. L. Boyce, “Increasing fracture toughness via architected porosity,” *Materials & Design*, vol. 205, p. 109696, 2021. [Online]. Available: <https://www.sciencedirect.com/science/article/pii/S0264127521002483>
 - [24] W. Lv, D. Li, and L. Dong, “Study on mechanical properties of a hierarchical octet-truss structure,” *Composite Structures*, vol. 249, p. 112640, 2020. [Online]. Available: <https://www.sciencedirect.com/science/article/pii/S0263822320302269>
 - [25] P. P. Indurkar, A. Shaikkea, Z. Xu, H. Cui, X. Zheng, and V. Deshpande, “The coupled strength and toughness of interconnected and interpenetrating multi-material gyroids,” *MRS Bulletin*, vol. 47, no. 5, pp. 461–473, 2022.
 - [26] M. Mirkhalaf, A. K. Dastjerdi, and F. Barthelat, “Overcoming the brittleness of glass through bio-inspiration and micro-architecture,” *Nature Communications*, vol. 5, no. 1, p. 3166, Jan 2014.
 - [27] M. Imam, J. Meaud, S. Ghosh, and T. Sain, “Improvement of stiffness and energy absorption by harnessing hierarchical interlocking in brittle polymer blocks,” *Journal of Applied Mechanics*, vol. 86, no. 5, p. 051007, 2019.
 - [28] M. E. Launey and R. O. Ritchie, “On the fracture toughness of advanced materials,” *Advanced Materials*, vol. 21, no. 20, pp. 2103–2110,

2009. [Online]. Available: <https://onlinelibrary.wiley.com/doi/abs/10.1002/adma.200803322>
- [29] . ASTM(E1820-23b), “Standard Test Method for Measurement of Fracture Toughness,” Tech. Rep., 2023.
 - [30] W. He, W. Luo, J. Zhang, and Z. Wang, “Investigation on the fracture behavior of octet-truss lattice based on the experiments and numerical simulations,” *Theoretical and Applied Fracture Mechanics*, vol. 125, p. 103918, 2023.
 - [31] B. Cotterell and J. K. Reddel, “The essential work of plane stress ductile fracture,” *International Journal of Fracture*, vol. 13, no. 3, pp. 267–277, Jun 1977.
 - [32] S. Liparoti, D. Sofia, A. Romano, F. Marra, and R. Pantani, “Fused filament deposition of pla: the role of interlayer adhesion in the mechanical performances,” *Polymers*, vol. 13, no. 3, p. 399, 2021.
 - [33] W. He, W. Luo, J. Zhang, and Z. Wang, “Investigation on the fracture behavior of octet-truss lattice based on the experiments and numerical simulations,” *Theoretical and Applied Fracture Mechanics*, vol. 125, p. 103918, 2023.
 - [34] A. J. D. Shaikeea, H. Cui, M. O’Masta, X. R. Zheng, and V. S. Deshpande, “The toughness of mechanical metamaterials,” *Nature materials*, vol. 21, no. 3, pp. 297–304, 2022.
 - [35] J. Hutchinson and Z. Suo, “Mixed mode cracking in layered materials,” ser. *Advances in Applied Mechanics*, J. W. Hutchinson and T. Y. Wu, Eds. Elsevier, 1991, vol. 29, pp. 63–191. [Online]. Available: <https://www.sciencedirect.com/science/article/pii/S0065215608701649>
 - [36] D. Bogy, “Edge bonded dissimilar orthogonal elastic wedges under normal and shear loadings,” *J. Appl. Mech.*, vol. 35, pp. 146–154, 1968.
 - [37] A. Evans, M. Rühle, B. Dalgleish, and P. Charalambides, “The fracture energy of bimaterial interfaces,” *Metallurgical Transactions A*, vol. 21, pp. 2419–2429, 1990.